

RESEARCH ARTICLE

Scalar dispersion by coherent structures in uniformly sheared flow generated in a water tunnel

Christina Vanderwel^{a*} and Stavros Tavoularis^b

^a*University of Southampton, Southampton, SO17 1BJ, UK;*

^b*University of Ottawa, Ottawa, K1N 6N5, Canada*

(submitted December 15, 2015)

In order to investigate the role of coherent structures as mechanisms of scalar dispersion, we studied measurements of a passive scalar plume released in a uniformly sheared turbulent flow generated in a water tunnel. The flow had homogeneous turbulence properties in the measurement domain and contained hairpin vortices similar to those in boundary layers, and so was an ideal test bed to study the effects of coherent structures on turbulent dispersion, free from the effects of inhomogeneities or boundaries. Measurements of the velocity and concentration fields were acquired simultaneously using stereo particle image velocimetry and planar laser induced fluorescence. We found that dye was preferentially located far away from vortices and was less likely to appear in close proximity to vortices, which is attributed to the high dissipation at the periphery of the vortices. However, we also found that dye was not directly correlated with the uniform momentum zones in the flow, suggesting a more complex relationship exists between these zones, the locations of vortices, and dye transport. Considering scalar flux events rather than simply the presence of dye as our condition of interest, a conditional eddy analysis demonstrated that hairpin vortices are responsible for the large scalar flux events as well as the large Reynolds stress events in the flow. The fact that the Reynolds stress was correlated with the scalar flux further confirmed that coherent structures are dominant mechanisms for scalar transport. Furthermore, we found that the scalar flux vector was preferentially inclined by 155° and -25° with respect to the streamwise direction, and was thus approximately orthogonal to the planes of the legs of the most common upright and inverted hairpin structures in the flow. These findings demonstrate that coherent structures play an important and intricate role in turbulent diffusion.

This is the Accepted Manuscript version of an article published by Taylor & Francis in the Journal of Turbulence in March 2016, available online: <http://dx.doi.org/10.1080/14685248.2016.1155713>.

Keywords: Passive Scalar Turbulence, Turbulent Mixing, Homogeneous Turbulence

1. Introduction

Coherent structures are the recurring, dominant, vortical, large-scale flow patterns that are ubiquitous in turbulent flows. Previous experimental and numerical studies have shown that hairpin vortices are the predominant coherent structures in turbulent boundary layers [1, 2] as well as in other shear flows [3, 4]. The generation of such structures has been explained by the lifting and stretching of quasi-two-dimensional roller vortices. Coherent structures have been shown to be a primary mechanism for the generation of Reynolds stresses that dominate the transport of momentum, so that their control has become an essential approach for drag and noise reduction.

*Corresponding author. Email: c.m.vanderwel@soton.ac.uk

As a corollary of Reynolds analogy, which connects heat and mass transport to momentum transport, one would expect that coherent structures should also be largely responsible for scalar transport. This connection has been demonstrated qualitatively by flow visualizations of scalar field patterns in turbulent boundary layers [5–7]. More recently, the presence of hairpin vortices has been observed in isocontours of a scalar field obtained by direct numerical simulations [2]. It has also been suggested that the uniform momentum zones that are created by hairpin vortex packets in turbulent boundary layers coincide with zones of uniform concentration [8, 9].

The effects of coherent structures on scalar transport are particularly important in the context of environmental flows. In the atmospheric surface layer, the ejection and sweep motions that are typically associated with coherent structures have been shown to be responsible for much of the land-surface evaporation, heat and momentum fluxes [10–14]. Coherent vortices have a significant impact in quasi-geostrophic flows in the ocean and the atmosphere; in such flows, scalars seeded within vortices were seen to experience lower dispersion than in the free stream, and to become, in a sense, islands of stability [15]. Investigations of particle dispersion have also demonstrated that coherent structures are responsible for particle clustering, which has direct ramifications to reactive flows such as combustion as well as to droplet coalescence and the formation of clouds in the atmosphere [16, 17]. A better understanding of the role of coherent structures in scalar transport is also important for the refinement of turbulent diffusion models.

In view of the importance of scalar dispersion in many applications, it is rather surprising that the role coherent structures play on the dispersion of passive scalars has not yet been studied quantitatively and systematically in the laboratory. The goal of the present work is to investigate both qualitatively and quantitatively the influence of coherent structures on turbulent dispersion. This work follows earlier studies of the diffusion of a plume of dye released from a point source in uniformly sheared flow (USF) generated in a water tunnel [18, 19]. The turbulence in fully developed USF is nearly homogeneous but strongly anisotropic, and has a large-scale structure that is dominated by hairpin-shaped vortices [3], comparable to those found in turbulent boundary layers. This article is an extended version of a paper presented recently at the TSFP-9 conference [20]; we have now included a more detailed description of our techniques, additional examples and discussion of the influence of vortices and updated several figures; most importantly, we have included new analysis of experimental results that document the role of uniform momentum zones that occur in USF as well as in turbulent boundary layers [1, 3, 9, 21–23] and have analyzed the orientation of the scalar flux vector with respect to the orientation of the coherent structures [3]. A description of the experimental apparatus and measurement techniques is provided in section 2. In section 3, we describe our analysis of the relative positions of dye patches, coherent vortices, and uniform momentum zones. In section 4, we analyze the scalar flux events, including a conditional eddy analysis to explore the mechanisms associated with instantaneous scalar flux events and a probabilistic analysis of the scalar flux vector orientation. We finish by summarizing our main conclusions.

2. Apparatus and flow conditions

Experiments were performed in the University of Ottawa’s recirculating water tunnel. Figure 1 presents a sketch of this experimental facility and the main instrumentation for this experiment. Uniform shear was generated in the test section of the water tunnel with the use of a shear generator located at the entrance to the

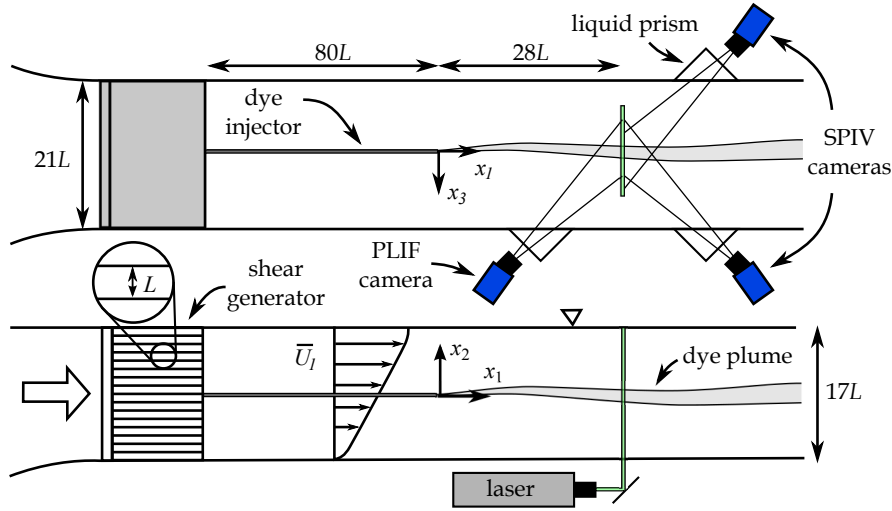


Figure 1. Top and side views of the experimental apparatus and main instrumentation in the water tunnel test section; $L = 25.4$ mm is the spacing of the shear generator.

test section. The mean and turbulent properties of the flow have been documented in detail in an earlier article [3]. The mean streamwise velocity at the centre of the channel was $U_c = 0.18$ m/s. All measurements were confined to the central core of the channel, within a domain of approximately $100 \text{ mm} \times 100 \text{ mm}$, which was located at least 150 mm away from any boundaries or the free surface. In this region, the mean velocity profiles were linear and the turbulence properties were nearly homogeneous on transverse planes. The turbulent stress tensor was strongly anisotropic and the turbulence Reynolds number was $Re_\lambda \approx 150$. The turbulence integral lengthscale was initially set by the shear generator spacing, $L = 25.4$ mm, and was much smaller than the dimensions of the flow domain.

Previous measurements in USF have documented the prevalence of hairpin-shaped vortices as the dominant coherent structures [3]. These structures have similar characteristics to those found in turbulent boundary layers at comparable Re_λ with an important difference: both upright and inverted hairpins have been observed in USF, with idealized shapes as illustrated in figure 2, whereas, in turbulent boundary layers, only upright structures exist, as the wall presumably suppresses the development of inverted hairpin vortices. Furthermore, in USF, coherent vortices are distributed evenly throughout the flow and are undisturbed by walls and intermittency. This makes USF an ideal test bed for studying the effects of coherent structures in the absence of extraneous effects.

In this experiment, an aqueous solution of fluorescent dye (Rhodamine 6G) with a source concentration of $C_S = 0.3 \text{ mg/l}$ was released isokinetically from a fine tube located in the centre of the tunnel in the fully developed region of the flow, where the turbulent kinetic energy and other properties grow exponentially [3, 24]. The density of the dye solution matched that of water so buoyancy effects were negligible. This dye has a Schmidt number of 2500 ± 300 [25], which implies that molecular diffusion was extremely weak and that the diffusion of the dye was dominated by turbulent motions.

Simultaneous measurements of the instantaneous velocity and concentration maps were obtained using stereoscopic particle image velocimetry (SPIV) and planar laser-induced fluorescence (PLIF) in planes normal to the flow direction. In this paper, we present measurements acquired at a distance of $x_1/L = 28$ from the tip of the injector nozzle, where the dye was dispersed significantly but remained relatively coherent so that it contained regions with relatively high concentration levels. The SPIV system provided maps of all three components of the turbulent

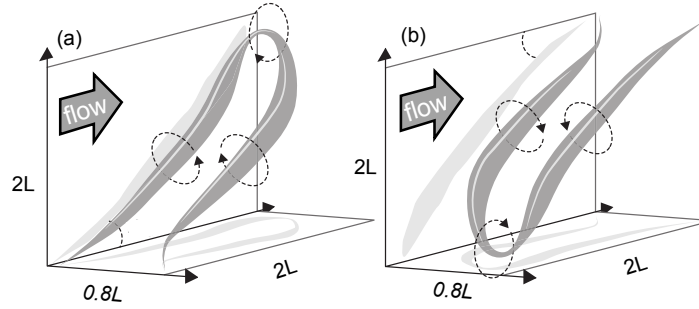


Figure 2. Sketches of (a) an upright and (b) an inverted hairpin vortex (adapted from [3]).

velocity and consisted of two cameras (Imager Pro X 4M, FlowMaster, LaVision) with illumination provided by a ND:YAG pulsed laser (Solo PIV 120XT, New Wave Research). In order to accommodate the oblique viewing angle required for taking measurements in cross-sections normal to the flow, all cameras were fitted with Schiempflug adapters; moreover, liquid prisms were used to prevent the optical aberrations due to horizontal astigmatism. Maps of the concentration were acquired using planar laser-induced fluorescence (PLIF) techniques from measurements of the dye fluorescence obtained with a third digital camera (PCO-Edge), synchronized with the SPIV system. This camera was fitted with a long-pass filter with a sharp cut-off at 540 nm in order to capture only the fluorescent light emitted by the dye. The intensity of the fluorescence was then converted to a concentration value, based on calibration measurements, which were performed before the experiment in a series of tanks; each tank contained dye with a uniform concentration and was in turn submerged in the water tunnel so that it occupied the same field of view as the one during plume measurements. Details of the measurement procedure and the plume characteristics have been published in previous articles [18, 19, 25].

3. The relative positions of dye patches, vortices and uniform momentum zones

As a first step towards identifying any possible connection of scalar dispersion to the actions of coherent structures, we investigated whether the locations of fluid marked by dye were correlated with or otherwise related to the locations of vortices and uniform momentum zones.

3.1. Vortex identification

The hairpin vortices in the present USF had wide ranges of orientation, but, most frequently, their axes were found to be nearly parallel to the $x_1 - x_2$ plane. Thus, the intersections of the cores of these vortices and the presently used sheet of light, which was parallel to the $x_2 - x_3$ plane, were expected to have nearly elliptical shapes. This expectation formed the basis for developing an algorithm that was applied to the SPIV velocity maps and was capable of identifying the locations, strengths and orientations of vortices in the flow. Following the method described in [3, 26, 27], this algorithm identified “cores” of vortices as regions of the flow where the swirling strength λ_{ci} exceeded a specified threshold λ_{th} . The swirling strength was determined with the same spatial resolution the velocity measurements. In the

present analysis, the threshold was defined as

$$\lambda_{\text{th}} = 10\lambda_{ci,av} \quad , \quad (1)$$

where $\lambda_{ci,av}$ was the local average swirling strength, which was determined by ensemble-averaging 500 independent measurements. The use of this threshold excluded small vortices and identified only the strongest vortices in the flow, thus meeting our objective to consider only large vortices. The cross-sectional area of each vortex core was subsequently determined by an area-growing part of the algorithm as the region around each core in which the swirling strength exceeded a boundary threshold of

$$\lambda_b = 0.2\lambda_{\text{th}}. \quad (2)$$

Then, an ellipse with the minimum area was fit to the boundary of each vortex core, the vortex centre was identified as the mid-point between the two foci of the ellipse and the vortex core diameter was defined as the average of its major and minor axis lengths. The sensitivity of the vortex core diameter estimate to the value of the boundary threshold was determined by repeating the analysis with a 100% higher value of λ_b ; this resulted in a mere 20% decrease in the average vortex diameter, which was deemed sufficiently small for the present purposes. Overall, we found that this method successfully distinguished neighbouring vortices, especially pairs of counter-rotating vortices, which were presumably the two legs of hairpin vortices; the two vortices in such pairs had vorticities of opposite signs and were separated by regions in which the swirling strength was negligible.

Figure 3 illustrates the various steps of this algorithm by a representative example. Figure 3a is a map of instantaneous in-plane velocity vector projections on the $x_2 - x_3$ plane, coloured by the streamwise velocity magnitude. Figure 3b illustrates the corresponding swirling strength map, which is used to identify the discrete vortices present. Finally, figure 3c shows the identified vortices superimposed on the original streamwise velocity map; the vortices are enclosed by fitted ellipses and velocity vectors within each vortex are presented relative to the convection velocity of each vortex to illustrate the direction of local rotation. As demonstrated in this example, the vortices were roughly evenly distributed throughout the flow, in concordance with the homogeneity of the turbulence. Several pairs of counter-rotating vortices are apparent, which are interpreted as cross-sections of hairpin vortices. One particularly strong vortex pair is shown to induce displacement of low-speed fluid towards a region of higher velocity.

3.2. *The locations of dye patches vis-à-vis the locations of vortices*

The complex relationship between the locations of vortices and the presence of dye is demonstrated in figure 4, which consists of four representative instantaneous snapshots of the concentration field, together with the vortices that were identified from the simultaneous velocity measurements. These snapshots were chosen to contain at least one strong pair of vortices (a.k.a. the legs of a hairpin vortex) in the vicinity of a vivid dye patch. Two different patterns of forceful scalar transport enacted by these vortices can be seen readily in these figures. In the first pattern, illustrated in figures 4b and c, dye surrounded one or both legs and occupied much of the space between them; it is presumed that these images correspond to dye that happened to be injected so that it marked some fluid in the “base” of the vortex, which in time got induced to move between the pair, following the

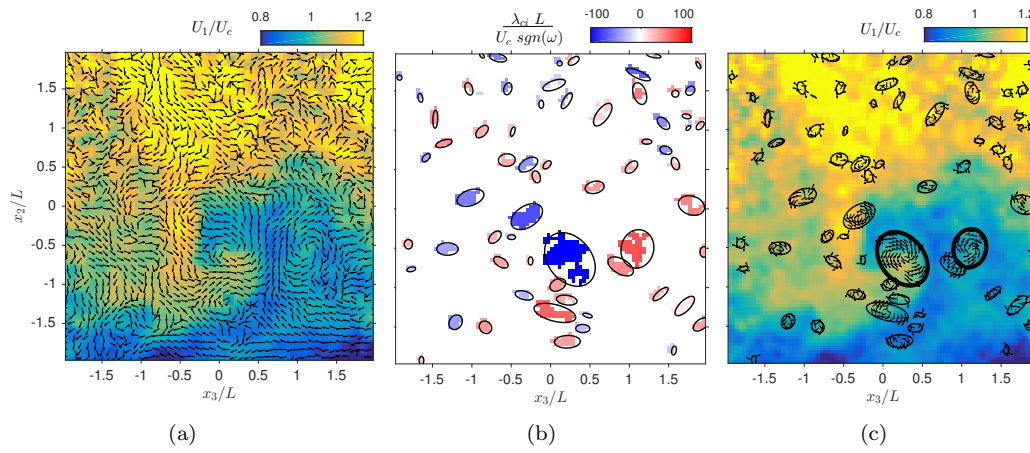


Figure 3. A representative illustration of the main steps of the vortex identification algorithm. (a) Instantaneous map of in-plane velocity vectors with superimposed flood contours of the streamwise velocity; the direction of the x_1 axis is out of the page. (b) Isocontours of swirling strength multiplied by the sign of vorticity; contours of ellipses fitted to regions with significant swirling strength are shown and assumed to demarcate vortex cores. (c) Vortices identified in (b) are shown together with local maps of the in-plane projections of the velocity vector relative to the vortex convection velocity; flood contours of the streamwise velocity are shown as well; bold ellipses mark a strong counter-rotating vortex pair and may be construed as the cross-sections of the legs of a hairpin vortex, which induces upwards motion of low-speed fluid.

direction of the arrows drawn in the plots. In the second pattern, illustrated in figures 4a and d, dye occupied mostly space away from the vortices in the direction of the induced motion of the fluid; it is presumed that these images correspond to dye that happened to be injected so that it marked fluid that was on the other side of the vortex base and so it did not pass between the pair but was instead displaced further away by fluid that did. All four examples are evidence that hairpin vortices vigorously transported dye in a manner that was consistent with their orientations, thus making strong contributions to its dispersion. Nevertheless, it was also realised that observation of dye patches alone could not reveal consistently the locations of these vortices, because the dye injection process was independent of the vortex generation mechanism and so the initial relative positions of dye patches and vortices were random. Statistical analysis of simultaneous swirling strength and concentration maps further showed that there was no significant cross-correlation between dye concentration and vortex locations.

3.3. The proximity of dye to vortices

To further investigate any possible relationship between the locations of regions containing dyed fluid and the locations of vortices, we calculated the average local volume fraction $\chi(r)$ of dyed fluid, as a function of distance r from the nearest vortex centre. This property is deemed to indicate the likelihood of dye presence at the given distance. To calculate $\chi(r)$, we first identified the vortex that was nearest to each pixel in the measurement domain and then determined the distance between the pixel and the vortex centre. Finally, we computed the volume fraction as

$$\chi(r) = \frac{N(r|C > 0)}{N(r)} . \quad (3)$$

This parameter represents the ratio of the number of pixels $N(r)$ located at a distance r from the nearest vortex centre that had non-zero concentration and the total number of pixels located at that distance. The corresponding results are

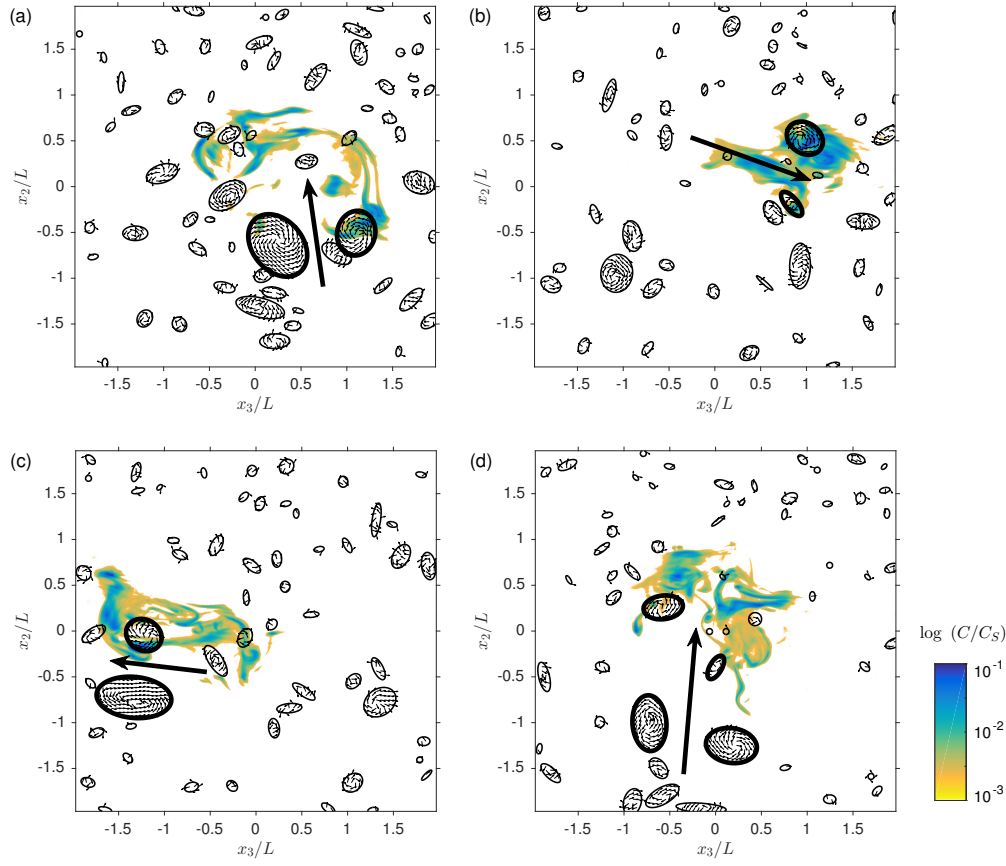


Figure 4. Four representative instantaneous maps illustrating the influence of coherent structures on dye transport. Plot (a) corresponds to the same instant as figure 3. Colour contours mark the concentration field in a logarithmic scale. Vortices are indicated by ellipses, with vectors indicating the local in-plane relative velocity. Pairs of relatively strong counter-rotating vortices, marked by bold ellipses, are generally seen to induce flows which displaced dyed fluid.

presented in figure 5, in which we normalized r by the mean vortex radius $\bar{R} = 0.07L$ and $\chi(r/\bar{R})$ by the overall volume fraction $\bar{\chi}$ in the entire measurement domain.

The likelihood of dye presence was lowest at the edge of the vortex, where the circumferential velocity was highest. This indicates that there was some segregation of dye in the core of the vortex as well as a tendency for dye to move away from the core. On the other hand, the likelihood of dye presence changed only slightly across the flow, which is consistent with the observed lack of significant correlation between dye concentration and vortex location. The trend of dye volume fraction can be explained by the following conjecture: dye that was injected into the vortex core would generally stay in the core, whereas dye that was injected outside the core could be wrapped around it or pushed away by transverse motions induced by a vortex pair, without penetrating the vortex core. Because flow regions between hairpin vortices are known to have, in general, nearly uniform momentum [3], it seems worthwhile to examine a possible relationship between dye patches and uniform momentum zones; this will be the subject of the remainder of this section.

3.4. Uniform momentum zone identification

The term Uniform Momentum Zones (UMZs) has been used to describe regions of relatively uniform velocity, which have been observed to appear in the centres of packets of quasi-streamwise hairpin vortices in turbulent boundary layers [1, 21–23, 28]. Turbulent boundary layers contain a hierarchy of UMZs, with typically two

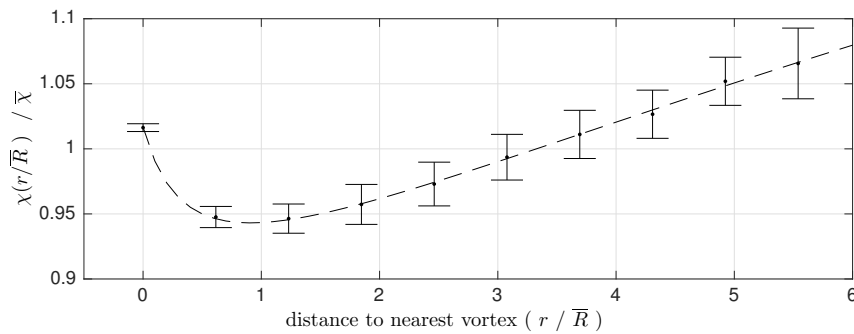


Figure 5. Dependence of the normalized average local volume fraction of dye on the normalized distance from the nearest vortex centre; uncertainty bars indicate the standard deviations of measurements at streamwise positions having $x_1/L = 20, 28$, and 35 .

to five UMZs across their thickness at any given time; the size of these zones has been seen to increase with wall-normal distance [23]. Most previous investigations identified UMZs by analysing instantaneous velocity maps that extended from the wall to the edge of the boundary layer, thus capturing all UMZs to their full wall-normal extents. The range of possible velocities in each map was bounded from below by zero and from above by the freestream velocity. In such cases, histograms of the values within each instantaneous streamwise velocity map exhibited well-defined local peaks, which were then unambiguously construed as the nominal velocities within different UMZs [21–23].

UMZs are also known to appear in USF, separated by shear layers containing vortices [3]. Nevertheless, unlike turbulent boundary layers, USF is not subjected to the bounding effects of the wall and the freestream. As a result, the identification of UMZs in the present USF as peaks in histograms of the instantaneous streamwise velocity was unsuccessful and needed to be adapted to the particular conditions of UMZs in USF. To illustrate this procedure, figures 6a,d present two representative instantaneous streamwise velocity maps, taken at the same instants as the plots shown in figures 4a,b. The corresponding velocity histograms, namely the probability density functions (PDFs) of the streamwise velocity $P(U_1)$, are shown in figures 6b,e. Unlike UMZs in turbulent boundary layers, UMZs in USF appeared at random transverse locations with respect to the map boundaries and those that occurred near the edges of the map often extended beyond the considered domain. Consequently, peripheral UMZs contributed fewer values to the population used for computing the histogram than centrally located UMZs and histogram peaks corresponding to peripheral UMZs were difficult to distinguish because they were much smaller than central peaks. This problem was exacerbated by the fact that the velocity in USF was unbounded on both sides and so the histograms had long tails, corresponding to fluid with velocities that were significantly higher or lower, respectively, than the averages at the upper and lower edges. Clear evidence for the bias in favour of central UMZs is provided in figures 6b,e by the bell-shaped appearance of the time-averaged PDF, $\overline{P(U_1)}$, calculated by averaging the PDF of 500 different snapshots. To compensate the instantaneous histograms for this bias, we have normalized them by $\overline{P(U_1)}$. The peaks of the corresponding compensated histograms, shown in figures 6c,f, have been construed to indicate the velocities of the UMZs in the present USF. Had the PDFs not been corrected for this bias, UMZs located at the edges of the domain would not have been identified. The boundaries between adjacent UMZs have been defined as the halfway points between these peaks [23] and contours at the boundary velocity values have been drawn in the velocity maps (figures 6a,d) as thin black lines. In both examples

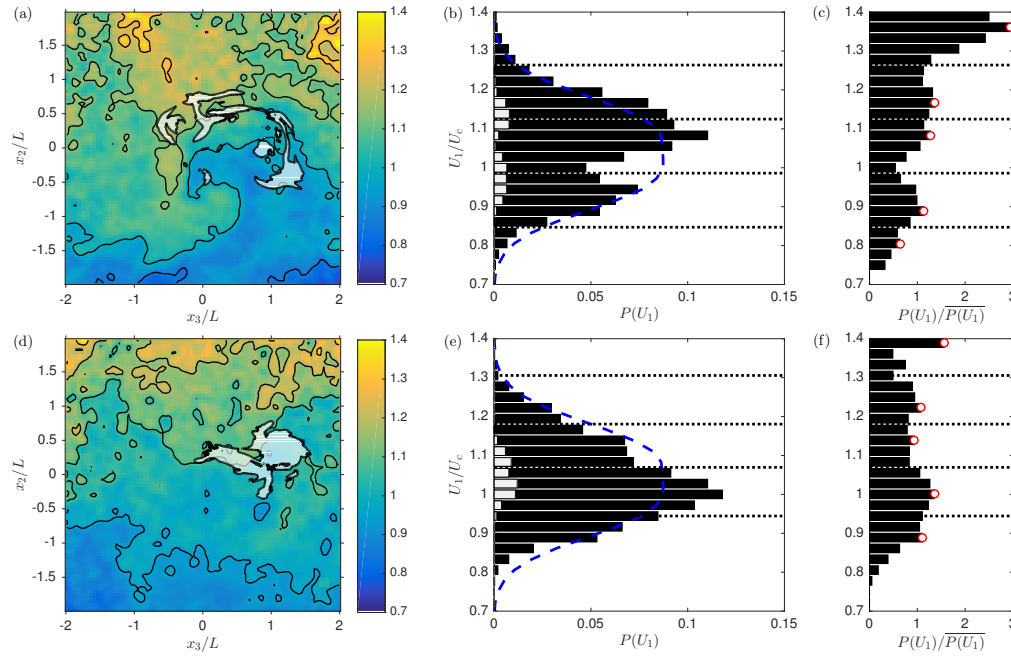


Figure 6. (a,d) Two representative instantaneous flood maps of the normalised streamwise velocity U_1/U_c with superimposed dye patches, shown as white regions; thin black lines mark the boundaries between uniform momentum zones (UMZs). (b,e) Instantaneous histograms (PDF) $P(U_1)$ of the streamwise velocity, in the form of black-bar plots, together with white bars indicating the portion of each black bar that corresponds to dyed fluid; the time-averaged PDF $\bar{P}(U_1)$ is indicated by a dashed blue line. (c,f) Relative histograms $P(U_1)/\bar{P}(U_1)$ normalised by $\bar{P}(U_1)$; peaks marked by red circles are construed to be UMZs, with their boundaries marked by dotted black lines.

shown, five UMZs were detected resulting in four bounding lines appearing on the velocity maps. Though the highest velocity UMZ occupies only a very small area in each image, these zones undoubtedly extend further outside the measurement domain.

3.5. The locations of dye patches vis-à-vis uniform momentum zones

Several previous investigations have suggested that dye distribution is connected with UMZs [8, 9], but a rigorous analysis of the relationship between scalar transport and UMZs has yet to be presented. In particular, Michioka and Sato [8] noted in their large-eddy simulation of a two-dimensional street canyon that instantaneous concentration contours often coincided with regions of low-momentum fluid. In addition, Eisma *et al.* [9] observed that the concentration field of dye released passively within a turbulent boundary layer in a water tunnel exhibited zones of uniform concentration that roughly overlapped with UMZs. In both of these cases, the scalar was released close to the wall and permeated the entire boundary layer. As both hairpin packets and UMZs originate from the near-wall region [21], it seems possible that, in these studies of boundary layers, dye was collected inside UMZs during their generation and remained within them as they moved away from the wall.

In the present case of a USF, UMZs were distributed randomly throughout the flow domain and had no systematic connection with the injection point of the dye. The purpose of our analysis was therefore to test whether dye was preferentially located within UMZs, despite the fact that the dye injection source was unrelated to the source of the UMZs. A prevalence of dye inside UMZs, by comparison to

that in the background turbulence, would suggest that UMZs have an inherent mechanism that is capable of attracting and retaining dye, irrespectively of its injection characteristics.

In order to obviate any possible relationship between the UMZs and the dye, we have superimposed the regions containing fluid with a non-zero dye concentration on the velocity maps in figures 6a,d. In neither example was the dye confined within a single UMZ. In figure 6a, dye appeared within three different UMZs, in rough alignment with the UMZ interfaces. In figure 6d, a large portion of the dye was concentrated near the edge of the central UMZ, which had a velocity that was approximately equal to the centreline average, but some dye also spilled into the adjacent UMZ, which was at a slightly higher velocity. We found that the patterns observed in these two examples were very common and that, while large portions of the dye were often contained within UMZs, the boundaries of the dye patches consistently appeared to follow the folds of the interfaces along the shear layers that separated the UMZs. The fact that the dye did not necessarily remain contained within a single UMZ, but was able to spill over into adjacent UMZs as well, is also illustrated by the fact that the velocity histograms $P(U_1|C > 0)$ of dye-containing fluid, shown as white bars in figures 6b,e, overlapped with more than one UMZs.

3.6. Further discussion

The previously presented analysis of simultaneous velocity and concentration maps has identified no measurable correlation between the locations of dye patches and either hairpin vortices or UMZs. Before speculating whether this observation would also apply to other types of scalar fields that may be superimposed passively to a shear flow, we must consider the particular conditions for the present scalar injection. Unlike some other experimental studies, the injected scalar plume in the present flow was particularly slender and so only a very small portion of each cross section of the flow was at any time occupied by fluid containing the scalar. If a larger quantity of dyed fluid were injected from a single or multiple ports, then more dye would be inevitably get trapped into vortex cores or UMZ central regions, where it would remain visible over a long distance from its source, because of the limited interactions between these regions and the remainder of the flow and the low molecular diffusivity of this particular substance. In contrast, dye injected outside these regions would likely get dispersed relatively fast and would not remain coherent. In such cases, observation of dye patterns away from the source may generate the impression that dye was transported preferentially into vortex cores and/or UMZs, which may not actually be the case.

Focusing on the UMZs, we may speculate that, because they exhibit nearly uniform momentum, they would also transport a passive scalar nearly uniformly. In turbulent boundary layers, uniform momentum zones are associated with low-speed streaks [1] that would induce a scalar flux against the direction of the flow, when considering a frame of reference moving with the mean convection velocity of the flow; however, in USF, the UMZs may either be high-speed regions or low-speed regions, depending on whether they are formed by upright or inverted hairpin packets [3] and may therefore induce scalar flux towards either upstream or downstream. Regardless of the direction of transport, the UMZs also behave as zones of nearly uniform scalar flux. It follows that the value of the scalar concentration within each UMZ would depend largely on the nature of the source of the scalar and the relative sparsity of the scalar in the flow. In the present experiments, the plume was very slender and the concentration field was very sparse, and, therefore, when dye happened to coincide with UMZs, it would likely be transported across them

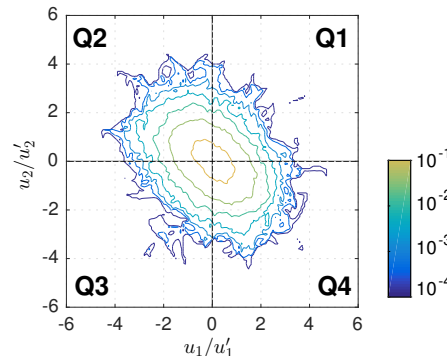


Figure 7. Contours of the joint probability density function of the streamwise and transverse velocity fluctuations (u_1 and u_2 , respectively), illustrating the predominance of Reynolds stress events to the Q2 and Q4 quadrants; primes indicate standard deviations.

and build up at their edges. If the concentration field were more widespread, as in the previous experiments in boundary layers [8, 9], this region of uniform transport might appear as a zone of nearly uniform concentration, and concentration gradients would tend to build up at the edges of the UMZs, where changes to flux vector occurred.

Our finding that the locations of coherent structures were not correlated with locations of fluid containing the scalar does not necessarily contradict Reynolds' analogy, which was meant to relate the magnitudes of momentum and scalar fluxes. The current location of a scalar patch would be the cumulative result of all motions it encountered since its injection into the flow, including those induced by multiple coherent structures, whereas the coherent structures are distributed randomly throughout the flow domain and are unaffected by the scalar presence. To better understand the complex relationship between coherent structures and the scalar field, we will now turn our focus to the scalar flux events themselves.

4. Analyzing the scalar flux events

Having demonstrated that the presence of dye was not a sensitive indicator of turbulent diffusion mechanisms in the present flow, we now turn our focus to the analysis of strong scalar flux events. Because we collected simultaneous measurements of all three velocity components and the concentration, we were able to reconstruct the instantaneous scalar flux vector $cu_i, i = 1, 2, 3$.

4.1. Conditional eddy analysis

Conditional eddy analysis is a method capable of reconstructing representative instantaneous flow patterns associated with the occurrence of significant flow events. This approach has been used by previous authors [1, 29] to identify large-scale coherent structures in the turbulent boundary layer, as patterns that occurred when the nearby flow field met the condition of a large Reynolds stress; reconstruction of the mean flow field resulted in a pattern that had the shape of a typical hairpin vortex.

In the present work, we first adapted conditional eddy analysis for vortex identification in USF and then extended it, for the first time, for identification of scalar transport events. As in turbulent boundary layers, in USF, the Reynolds stress tensor is anisotropic and the joint PDF of the streamwise and transverse velocity fluctuations (see figure 7) indicates a proclivity for events in the Q2 ($u_1 < 0$ and

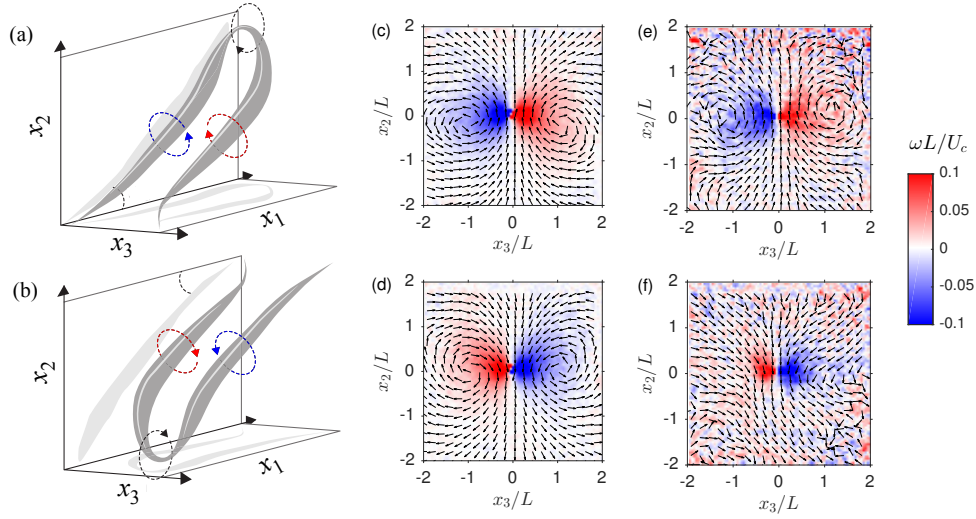


Figure 8. Vorticity maps of the conditionally averaged flow fields based on the presence of (c) large Reynolds stress events in Q2 and (d) in Q4 and (e) large positive values of cu_2 and (f) large negative values of cu_2 . The flow fields indicate the presence of counter-rotating vortex pairs corresponding with the cross-sections of (a) upright and (b) inverted hairpin vortices.

$u_2 > 0$) and Q4 ($u_1 > 0$ and $u_2 < 0$) quadrants, known as ejections and sweeps, and which is consistent with the negative correlation between u_1 and u_2 . It is noted that, unlike turbulent boundary layers in which a one-sided (“upright”) orientation of hairpin vortices is imposed by the wall, USF has hairpins in both “upright” and “inverted” orientations [3]. For this reason, and following [30], we identified large Reynolds stress events in both the Q2 and the Q4 quadrants as those that met the condition

$$|u_1 u_2| > 4u_1' u_2' . \quad (4)$$

Subsequently, the instantaneous velocity field in the vicinity of each identified event was shifted so that the origin of its coordinates coincided with the location of the event. Finally, the conditional flow field was determined as the ensemble average of all shifted instantaneous flow fields. In addition to this approach, we have also applied an alternative one, namely Linear Stochastic Estimation (LSE) [31], and found essentially equivalent results.

The corresponding conditionally averaged flow fields in the cross-sectional planes normal to the flow are shown in figures 8c,d. Both flow fields are cross-sections of pairs of counter-rotating vortices with sizes comparable to the characteristic lengthscale L and consistent with the signatures of a hairpin vortex. Q2 events (*i.e.*, ejections) correspond to upright hairpin vortices (figure 8a), whereas Q4 events (*i.e.*, sweeps) correspond to inverted hairpin vortices (figure 8b).

Subsequently, we determined the conditional eddies that met the scalar flux condition

$$|cu_2| > 4c' u_2' , \quad (5)$$

where c is the dye concentration fluctuation. The resulting flow field associated with large positive cu_2 events (figure 8e) clearly indicates a pair of counter-rotating vortices corresponding to an upright hairpin vortex, which is also associated with large Reynolds stress events in the Q2 quadrant (*i.e.*, ejections). The flow field associated with large negative cu_2 events (figure 8f) is consistent with the presence of inverted hairpin vortices, which are also associated with large Reynolds stress

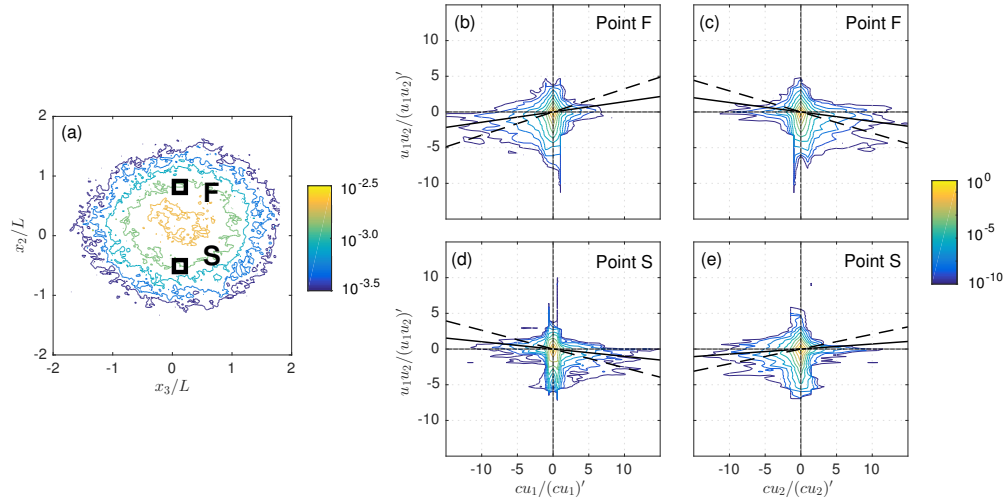


Figure 9. (a) Contours of the mean concentration \bar{C}/C_S with the two regions of interest indicated by squares. (b-e) Joint PDFs of the streamwise cu_1 and transverse cu_2 scalar fluxes and the Reynolds stress u_1u_2 , measured at points F and S and normalized by the corresponding standard deviations. The solid lines indicate the correlation coefficients whereas the dashed lines indicate the correlation coefficients determined from values conditioned on $C > 0$.

Table 1. Values of the correlation coefficient between the scalar flux components cu_i and the Reynolds stress u_1u_2 .

Point	Scalar flux component	ρ	$\rho (C > 0)^a$
F	cu_1	+0.14	+0.33
F	cu_2	-0.13	-0.30
S	cu_1	-0.10	-0.26
S	cu_2	+0.07	+0.21

^a The correlation coefficient determined from values conditioned on $C > 0$.

events in the Q4 quadrant (*i.e.*, sweeps). The conditional eddies identified by the large scalar flux condition appear to be less distinct than those identified by the large Reynolds stress condition; this difference is attributed to the fact that scalar flux events were restricted only within the present slender plume, whereas Reynolds stress events occurred in the entire flow domain. Nonetheless, these results demonstrate the link between Reynolds stress events, scalar flux events, and the coherent structures in the flow. A similar connection between Reynolds stress events and scalar transport has been found in simulated atmospheric boundary layers over canopies, in which large sweep and ejection events were a major source of scalar transport across the canopy [10, 12]; when large Reynolds stress events happened to occur near scalar interfaces, they generated regions with a large scalar gradient, called “scalar microfronts” [13]. based on the results of the present conditional eddy analysis, we may confidently include uniformly sheared turbulent flows to the list of flows in which coherent vortices are a dominant mechanism for turbulent scalar transport.

4.2. Correlations between Reynolds stress and scalar flux

In support of the previous assertion, we investigated the possible correlation between the Reynolds stress and the scalar flux. We present representative measurements at two locations on either side of the axis of the plume, along the mean velocity gradient direction, near the two inflection points of the mean concentration profile (points F and S, respectively, as indicated in figure 9a). The joint PDFs of the scalar fluxes and the Reynolds stress are presented in figure 9b-e. At point

F, the joint PDF of cu_1 and u_1u_2 is clearly biased to the third quadrant, indicating a positive correlation between the Reynolds stress and the streamwise scalar flux. The joint PDF of cu_2 and u_1u_2 is clearly biased to the fourth quadrant, indicating a negative correlation. Similarly at point S, the joint PDF of cu_1 and u_1u_2 is biased to the fourth quadrant, indicating a negative correlation, whereas the joint PDF of cu_2 and u_1u_2 is biased to the third quadrant, indicating a positive correlation. The change of sign of the correlations at points F and S is consistent with the change of sign of the mean scalar fluxes at these points. The fact that the correlations involving cu_1 and cu_2 have opposite signs is consistent with the fact that the streamwise and transverse scalar fluxes are negatively correlated at these locations [18]. The values of the correlation coefficients are presented in table 1 and are also indicated by lines in figure 9. The fact that the magnitudes of these correlation coefficients were fairly low is attributed to the highly intermittent nature of the present plume, which is a consequence of its slenderness; therefore, correlation coefficients were also determined considering only fluid that contained some dye ($C > 0$). The resulting conditional correlation coefficients were significantly larger in magnitude than the unconditional ones, which further supports the conjecture that coherent structures simultaneously transport both mass and momentum. We note that significant correlations between the Reynolds stress and the fluxes of heat and water vapour were also observed by Li & Bou-Zeid [11] in the atmospheric surface layer.

4.3. The orientation of the scalar flux vector

As we measured all components of the scalar flux vector $cu_i, i = 1, 2, 3$, we were also able to determine its instantaneous orientation. We defined the direction of the local scalar flux vector by the angle α between the projection of this vector on the (x_1, x_2) plane and the streamwise direction x_1 and the angle β between this vector and the (x_1, x_2) plane, as illustrated in figure 10. We then computed the conditional probability density functions (PDFs) of these two angles, under the condition that the magnitude of the scalar flux vector was larger than a specified threshold. The calculations were performed over an ensemble of 1000 instantaneous maps of the scalar flux vector, each containing 1857×1857 values; these maps were constructed from simultaneous maps of concentration, which had the finer resolution, and coarser velocity maps that were resampled and interpolated at this finer resolution; interpolation was justified by the fact that the resolution of the velocity measurements was very close to the Kolmogorov lengthscale of the flow [3]. Figure 10 shows four sets of these PDFs for thresholds of the scalar flux correlation coefficient magnitude equal to 0, 2, 10 and 30. As the threshold was increased, the level of the conditional PDF was decreased, as a result of the decreasing sample population. In the cases with the largest threshold, this population consisted of only about 1 in 20000 of the total sample size and, as a result, the corresponding PDFs had visible scatter. In general, and despite the increasing scatter, as the threshold was increased, the shapes of the PDFs of both angles were maintained and in fact became more accentuated. The PDF of α had two mildly sharp peaks at about -25° and 155° , whereas the PDF of β was symmetric about zero, where it peaked only slightly, maintaining nearly uniform values over a wide range of angles. The two prevalent orientations of the scalar flux vector were roughly normal to the prevalent orientations of the upright and inverted hairpin vortices, which, as observed in our previous study, were typically inclined by 35° and -145° , respectively, with respect to the streamwise axis and located symmetrically with respect to the (x_1, x_2) plane [3].

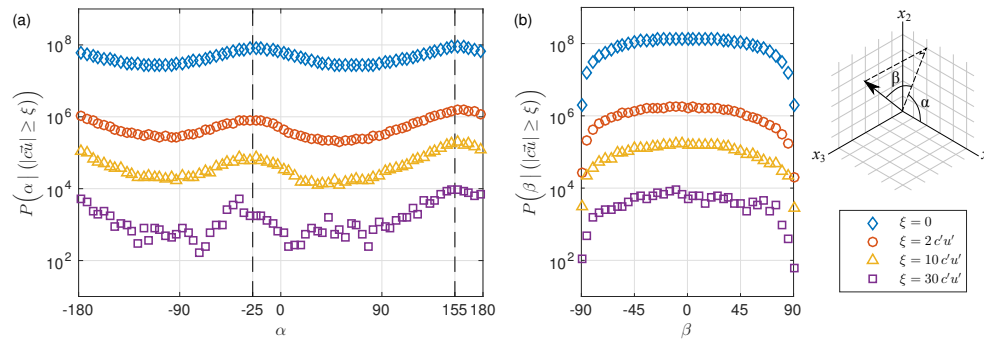


Figure 10. Conditional probability density functions of the two orientation angles of the instantaneous scalar flux vector.

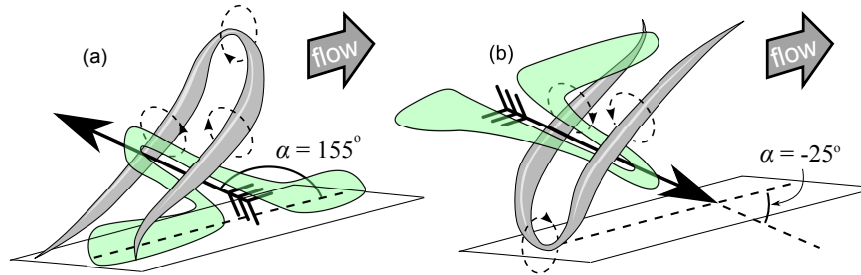


Figure 11. A model for scalar transport by upright (a) and inverted (b) hairpin vortices in USF.

Based on these observations, we may propose a model for scalar transport by hairpin vortices, as shown in figure 11. Scalar that happens to be just below an upright vortex, or just above an inverted one, is entrained into the motion that is induced by the two counter-rotating legs of the vortex [1] and gets extruded between the legs to the opposite side. Such events, although relatively sparse, are very strong and so influence significantly the overall scalar transport patterns, as evidenced by the presence of well defined peaks even in the unconditioned PDF of α .

In summary, the present analysis of scalar flux events has demonstrated that the actions of hairpin vortices are largely responsible for the generation of scalar flux in USF, in a manner analogous to the generation of Reynolds shear stress. We would expect this to be true also for turbulent boundary layers and other turbulent shear flows in which hairpin vortices are predominant.

5. Conclusions

The influence of coherent structures on turbulent dispersion of passive scalars was investigated, both qualitatively and quantitatively, through analysis of simultaneous measurements of the instantaneous concentration and velocity fields in a dye-marked plume. Despite the absence of a direct correlation between the scalar concentration and the locations of coherent vortices, dye was found to segregate preferentially within vortex cores and away from vortices and less likely to be present in the periphery of vortices. Similarly, an analysis of the location of dye vis-à-vis uniform momentum zones yielded no direct correlation, but dye appeared to be transported across the UMZs and build up along their boundaries. We noted that the observed patterns were particular to the present localised dye-injection procedure and the sparsity of the present scalar field; we suggested that, had we

instead introduced dye in bulk, we may have observed a tendency for zones of uniform concentration to coincide with UMZs.

Scalar flux measurements were analysed statistically. A conditional eddy approach demonstrated that counter-rotating vortices, which constitute the legs of hairpin vortices, were responsible for the strong scalar flux events in the flow. The scalar flux was found to be correlated strongly with the Reynolds shear stress. Finally, an analysis of the orientation of the scalar flux vector confirmed a prevalence to angles of 155° and -25° , which are approximately orthogonal to the planes of the upright and inverted hairpin structures in the flow. These results demonstrate that coherent structures are the main cause of large scalar flux events and play a dominant role in turbulent diffusion.

Acknowledgements

Financial support by the Natural Sciences and Engineering Research Council of Canada (NSERC) is gratefully acknowledged.

References

- [1] R.J. Adrian, *Hairpin vortex organization in wall turbulence*, Phys. Fluids 19 (2007), 041301, p. 041301.
- [2] X. Wu, and P. Moin, *Transitional and turbulent boundary layer with heat transfer*, Phys. Fluids 22 (2010), 085105, p. 085105.
- [3] C. Vanderwel, and S. Tavoularis, *Coherent structures in uniformly sheared turbulent flow*, J. Fluid Mech. 689 (2011), pp. 434–464.
- [4] S. Ghaemi, and F. Scarano, *Counter-hairpin vortices in the turbulent wake of a sharp trailing edge*, J. Fluid Mech. 689 (2011), pp. 317–356.
- [5] M.R. Head, and P. Bandyopadhyay, *New aspects of turbulent boundary-layer structure*, J. Fluid Mech. 107 (1981), pp. 297–338.
- [6] S.J. Kline, W.C. Reynolds, F.A. Schraub, and P.W. Runstadler, *The structure of turbulent boundary layers*, J. Fluid Mech. 30 (1967), pp. 741–773.
- [7] R.E. Falco, *Coherent motions in outer region of turbulent boundary layers*, Phys. Fluids 20 (1977).
- [8] T. Michioka, and A. Sato, *Effect of incoming turbulent structure on pollutant removal from two-dimensional street canyon*, Bound.-lay. Meteorology 145 (2012), pp. 469–484.
- [9] J. Eisma, J. Westerweel, and G.E. Elsinga, *Simultaneous scanning tomo-PIV and LIF in a turbulent boundary layer*, 11th International Symposium on Particle Image Velocimetry - PIV15, Santa Barbara, California, September 14-16 (2015).
- [10] G. Katul, G. Kuhn, J. Schieldge, and C.I. Hsieh, *The ejection-sweep character of scalar fluxes in the unstable surface layer*, Bound.-Lay. Meteorol. 83 (1997), pp. 1–26.
- [11] D. Li, and E. Bou-Zeid, *Coherent structures and the dissimilarity of turbulent transport of momentum and scalars in the unstable atmospheric surface layer*, Bound.-Lay. Meteorol. 140 (2011), pp. 243–262.
- [12] J. Huang, G. Katul, and J. Albertson, *The role of coherent turbulent structures in explaining scalar dissimilarity within the canopy sublayer*, Envl Fluid Mech 13 (2013), pp. 571–599.
- [13] J.J. Finnigan, R.H. Shaw, and E.G. Patton, *Turbulence structure above a vegetation canopy*, J Fluid Mech 637 (2009), pp. 387–424.
- [14] B.N. Bailey, and R. Stoll, *The creation and evolution of coherent structures in plant canopy flows and their role in turbulent transport*, J Fluid Mech 789 (2016), pp. 425–460.
- [15] A. Provenzale, *Transport by coherent barotropic vortices*, Annu. Rev. Fluid Mech. 31 (1999), pp. 55–93.
- [16] R.A. Shaw, W.C. Reade, L.R. Collins, and J. Verlinde, *Preferential concentration of cloud droplets by turbulence: Effects on the early evolution of cumulus cloud droplet spectra*, J. Atmos. Sci. 55 (1998), pp. 1965–1976.
- [17] D.W.I. Rouson, and J.K. Eaton, *On the preferential concentration of solid particles in turbulent channel flow*, J. Fluid Mech. 428 (2001), pp. 149–169.
- [18] C. Vanderwel, and S. Tavoularis, *Measurements of turbulent diffusion in uniformly sheared flow*, J. Fluid Mech. 754 (2014), pp. 488–514.
- [19] C. Vanderwel, and S. Tavoularis, *Relative dispersion of a passive scalar plume in turbulent shear flow*, Phys. Rev. E 89 (2014), p. 041005.
- [20] C. Vanderwel, and S. Tavoularis, *Scalar dispersion by coherent structures*, Ninth International Symposium on Turbulence and Shear Flow Phenomena - TSFP9, Melbourne, Australia, June 30 - July 3 (2015).
- [21] R.J. Adrian, C.D. Meinhart, and C.D. Tomkins, *Vortex organization in the outer region of the turbulent boundary layer*, J. Fluid Mech. 422 (2000), pp. 1–54.
- [22] Y.S. Kwon, J. Philip, C.M. de Silva, N. Hutchins, and J.P. Monty, *The quiescent core of turbulent channel flow*, J. Fluid Mech. 751 (2014), pp. 228–254.
- [23] C.M. de Silva, N. Hutchins, and I. Marusic, *Uniform momentum zones in turbulent boundary layers*, J. Fluid Mech. 786 (2016), pp. 309–331.

- [24] S. Tavoularis, and U. Karnik, *Further experiments on the evolution of turbulent stresses and scales in uniformly sheared turbulence*, J. Fluid Mech. 204 (1989), pp. 457–478.
- [25] C. Vanderwel, and S. Tavoularis, *On the accuracy of PLIF measurements in slender plumes*, Exp. Fluids 55 (2014).
- [26] J. Zhou, R.J. Adrian, S. Balachandar, and T. Kendall, *Mechanisms for generating coherent packets of hairpin vortices in channel flow*, J Fluid Mech 387 (1999), pp. 353–396.
- [27] P. Chakraborty, S. Balachandar, and R.J. Adrian, *On the relationships between local vortex identification schemes*, J Fluid Mech 535 (2005), pp. 189–214.
- [28] I. Marusic, *On the role of large-scale structures in wall turbulence*, Phys. Fluids 13 (2001), pp. 735–743.
- [29] R.J. Adrian, and P. Moin, *Stochastic estimation of organised turbulent structure: homogeneous shear flow*, J. Fluid Mech. 190 (1988), pp. 531–559.
- [30] R.A. Antonia, *Conditional sampling in turbulence measurement*, Annu. Rev. Fluid Mech. 13 (1981), pp. 131–156.
- [31] R.J. Adrian, *Stochastic estimation of conditional structure: a review*, Appl. Sci. Res. 53 (1994), pp. 291–303.